Spatial single-cell Organellomics reveals nutrient dependent hepatocyte heterogeneity and predicts pathophysiological status *in vivo*

Alexander Hillsley[1,2†], Raghabendra Adhikari [1†], Alana Dowdell Johnson[1,3], Isabel Espinosa-Medina[1], Jan Funke[1], Daniel Feliciano[1]*

[†] These authors contributed equally to this work.

[1]Janelia Research Campus, Howard Hughes Medical Institute; Ashburn, VA, 20147; USA.

[2] Chan Zuckerberg Biohub, San Francisco, CA, USA.

[3] Janelia-Meyerhoff Undergraduate Scholars Program 2024.

*Correspondence to: felicianod@janelia.hhmi.org

Abstract

Cellular heterogeneity within complex tissues and organs is essential to coordinate biological processes across biological scales. The effect of local cues and tissue microenvironments on cell heterogeneity has been mainly studied at the transcriptional level. However, it is within the subcellular scale - the organelles - that lays the machinery to conduct most metabolic reactions and maintain cells alive, ensuring proper tissue function. How changes in subcellular organization under different microenvironments define the functional diversity of cells within organs remains largely unexplored. Here we determine how organelles adapt to different microenvironments using the mouse liver as model system, in combination with computational approaches and machine-learning. To understand organelle adaptation in response to changing nutritional conditions, we analyzed 3D fluorescent microscopy volumes of liver samples labeled to simultaneously visualize mitochondria, peroxisomes, and lipid droplets from mice subjected to different diets: a control diet, a high-fat diet, and a control diet plus fasting. A *Cellpose* based pipeline was implemented for cell and organelle segmentation, which allowed us to measure ~100 different organelle metrics and helped us define subcellular architectures in liver samples at the single cell level. Our results showed that hepatocytes display distinct subcellular architectures within different regions of the liver -close to the central vein, in the middle region, and near the portal vein- and across the various diet groups, thus reflecting their adaptation to specific nutritional inputs. Principal component analysis and clustering of hepatocytes based on organelle signatures revealed 12 different hepatocyte categories within the different experimental groups, highlighting a reduction in hepatocyte heterogeneity under nutritional perturbations. Finally, using single cell organelle signatures exclusively, we generated machine learning models that were able to predict with high accuracy different hepatocyte categories, diet groups, and the stages of MASLD. Our results demonstrate how organelle signatures can be used as hallmarks to define hepatocyte heterogeneity and their adaptation to different nutritional conditions. In the future, our strategy, which combines subcellular resolution imaging of liver volumes and machine learning, could help establish protocols to better define and predict liver disease progression.

Introduction

Cellular heterogeneity establishes the structural basis of complex tissue architectures that allows cells to coordinate essential biological processes across biological scales (1,2). Most of these processes are regulated in discrete subcellular compartments that contain the required machinery to conduct metabolic reactions and keep cells alive, ensuring proper tissue function (3,4). Physiological challenges like altered nutrient concentration or oxygen levels trigger specific biochemical pathways in different subcellular structures, segregating cell tasks essential to adapt to distinct metabolic inputs and increasing the functional heterogeneity of tissues (5). Studies on the effect of local metabolic cues on cellular function have focused on how extrinsic signals regulate cell heterogeneity at the transcriptional level (6-8). However, how subcellular organization responds to different microenvironments and thereby expands the functional diversity of cells within organs remains largely unexplored.

How different microenvironments can influence the functional state of cells within a tissue is exemplified in the liver. Hepatocytes in the liver are organized into repeated hexagonal units known as liver lobules, which can be further divided into six hepatic acini, each being the smallest functional anatomical unit of the liver (9). This specific architecture forms a gradient of oxygen, nutrients and hormones generating different microenvironments where distinct populations of hepatocytes function together and give rise to a phenomenon known as "metabolic liver zonation" where liver tasks are compartmentalized in three liver zones (10-12).

At the subcellular level, organelles within hepatocytes respond to external signals regulating cellular bioenergetics, including detoxification and balance levels of lipids and glucose in the blood, essential to maintain bodily homeostasis (13). Different signals including nutritional cues have been shown to modify organelle morphology, numbers, and subcellular localization. These morphological changes directly correlate with the ability of organelles to perform specific tasks and meet the metabolic demands of the cell (14). Most of this knowledge has originated from fluorescence microscopy studies using tissue-culture systems, that combined with the implementation of machine-learning strategies expanded our basic understanding on how different organelles and their associated proteins respond to different signals (15, 16). However, the intricate regulation of organelle adaptive responses in vivo, in the context of the multiscale architecture of the liver is poorly understood.

Defects in organelle function in the liver are linked to metabolic diseases like Metabolic dysfunction-associated steatotic liver disease (MASLD), Type-2 diabetes and obesity (17, 18). Furthermore, previous studies indicate that the morphology of some organelles vary along hepatic acini after different nutritional regiments and oscillate during feeding-fasting cycles (19, 20). Overall, these studies suggest that the organization and characteristics of organelles within hepatocytes generate specific "signatures" that underlie the cellular functional heterogeneity required to sustain different metabolic states in health and disease. Recent studies assessing hepatocyte heterogeneity have mainly focused on differences in transcriptional signatures. However, these approaches involved tissue dissociation leading to cell loss and lack single cell spatial resolution (21-23). Another method used spatial proteomics to explore the proteome characteristics of different hepatocytes subpopulations maintaining both tissue context and single-cell resolution (24). While very powerful, this technique requires specialized instrumentation for cell capture microdissection and has a relatively low throughput (~500 cells). Microscopy approaches in combination with machine learning provide a high throughput alternative but have

not been implemented in the study of organelle adaptation at the single-cell level within complex tissue microenvironments including the liver's (16, 25). This is in part because imaging multiple organelles simultaneously within large tissue samples is challenging. Moreover, we still lack analysis pipelines with enough spatial resolution to resolve single-cell organelle signatures and define hepatocyte heterogeneities in the intact liver tissue context.

To overcome this challenge, we developed scOrganellomics, a fluorescent microscopy-based workflow including Python and Cellpose guided imaging analysis for the segmentation of three different organelles (peroxisomes, mitochondria, and lipid droplets) with single cell resolution in intact liver lobules. Using this approach we compared different experimental mice groups – mice on a control diet, a model of western diet (high-fat/high-carbohydrate diet), and a control diet combined with fasting- to study organelle adaptation in response to changing nutritional cues. Principal component analysis and clustering strategies of single hepatocyte organelle features defined 5 unique hepatocyte categories in control samples reflecting distinct subcellular architectures. Surprisingly, our results reveal that different hepatocyte categories co-exist within specific liver zones, except for hepatocyte category 5 which was only localized near the central vein. Analysis of livers from mice subjected to fasting or fed with a high-fat/ high-carbohydrate diet showed a significant reconfiguration of organelle features resulting in new hepatocyte categories (4 and 3, respectively) that displayed a less heterogenous distribution across the hepatic acinus compared to control liver samples. This highlights a previously overlooked hepatocyte heterogeneity which could help explain how the liver adapts to functional challenges across different microenvironments. Finally, using single-cell organelle signatures, we generated machine-learning models that were able to predict with high accuracy the different hepatocyte categories, the nutritional regiment used and the stage in the progression of early stage MASLD. Together, our results demonstrate that subcellular features in the form of organelle signatures can be used as hallmarks to define spatial hepatocyte heterogeneity during normal body physiology and early stages of metabolic diseases.

Results

scOrganellomics: a new method to investigate the spatial patterning of organelle structures in tissues.

We aimed to develop a method to study the spatial patterning of organelles in complex tissues, leveraging the principle that cellular responses are mediated by organelle adaptations to local microenvironments (26-28). To this end, we used the mouse liver as a model as this is a very organized tissue comprising hexagonal units – the hepatic lobules – where hepatocytes experience gradients of nutrients and signaling factors from the portal vein (PV) to the central vein (CV), leading to differential adaptation that creates a functional metabolic zonation (Fig. 1a) (9-12).

To determine the hepatocyte organelle structures at single-cell resolution within the liver tissue context, we developed a new pipeline for imaging, segmentation, and analysis of large liver tissue sections (Fig.1b). We focused on mitochondria, peroxisomes, and lipid droplets, as key organelles in metabolic responses (29, 30). To image hepatocytes and organelles, we use liver sections from male fed mt-Dendra2 transgenic mice expressing a fluorescent marker for mitochondria (34) and complementary immunostaining to visualize peroxisomes (PMP70 +), lipid droplets (LipidTOX) and the boundaries of hepatocytes (phalloidin). We confirmed accurate selection of hepatic lobules

including all 3 functional zones (Zone 1, Zone 2 and Zone3), staining liver sections in parallel for Aldolase B (highly expressed near the PV) and CYP2E1 (expressed in an opposite pattern, near the CV) (Fig.1c) (31, 32).

Using confocal microscopy, we captured high-resolution 3D images spanning three lobules per animal (three acini per lobule). Each of the lobules comprised an average of 450 hepatocytes across the PV-CV axis. In total we imaged more than 4000 hepatocytes and millions of organelles in our samples. Hepatocyte cellular and subcellular segmentation was performed using our new Python package, termed Liv-Zones (GitHub), and custom Cellpose-based models. Liv-Zones allows the segmentation of hepatocytes and organelles, extracting ~100 organelle metrics that are combined at the single-cell level thus providing for the first time a tissue-to-organelle scale context of liver zonation.

To evaluate differences in organelle distribution across the hepatic acinus, we organized our data based on cell position (20 bins) and visualized these using heatmaps. Our analysis shows zonated patterns of different mitochondria, peroxisome and LD features distributed across the PV-CV axis (Fig. 1d). Among these features we found that, for the most part, mitochondria and peroxisomes have correlated distributions, which agrees with their known interdependence relationship regulating lipid metabolism (33). Both mitochondria and peroxisomes where in higher number displaying mostly tubulated morphologies in hepatocytes near the CV compared to those close to PV. On the other hand, many of the LD features show opposite distributions when compared to distributions for mitochondria and peroxisomes features. These results indicate that the spatial patterns of organelle structures reflect the functional status of hepatocytes within defined liver zones. To further dissect subcellular differences across liver zones, we compared organelle features between zones using volcano plots. This analysis revealed that peroxisomes and lipid droplets accounted for 60% and 40% of the differences between zones 1 and 2, respectively, while peroxisomes and mitochondria contributed equally to differences between zones 1 and 3 (Fig. 2a).

Thus, our workflow, termed scOrganellomics, allows to investigate single-cell (sc) organelle structures spatially within complex tissue microenvironments such as the liver. Further, our results suggest that organelle signatures can be used as hallmarks of the functional heterogeneity of hepatocytes in the liver.

Organelle signatures define hepatocyte categories and reveal cellular heterogeneity within liver zones.

Based on our previous results, we sought to test whether organelle signatures could reveal hepatocyte subclasses within liver zones. To this end, we implemented Principal Component Analysis (PC1: 29% variance, PC2: 12% variance) and Gaussian Mixture Models (GMM) to cluster hepatocytes based on organelle features and visualized five distinct hepatocyte categories (H1–H5) (Fig. 2b). These five hepatocyte categories exhibited unique properties of mitochondrial, peroxisomal, and lipid droplet features (Fig. 2c), driven by the dominance of specific organelle subtypes (Fig. 2d). As an example, H1 hepatocytes had a high proportion of large and round mitochondria which localize closer to the center of the cell near the nucleus, while H5 showed the opposite trend (Fig. 2c, d). This suggests these categories represent hepatocytes with distinct metabolic demands residing within different liver microenvironments.

To map the position of hepatocyte categories along the PV–CV axis in the context of our GMM clustering analyses, we color-coded hepatocyte from all categories based on their position within the hepatic acinus and measured the frequency for each category to localize within different regions (Fig. 2e). Our analysis revealed differential distributions across the acinus, with some categories (H1, H2, H3) biased toward the PV and others (H4, H5) toward the CV (Fig. 2e). Surprisingly, analysis of hepatocyte category distribution within the three liver zones (Z1-Z3) revealed hepatocyte category heterogeneity within each zone, with Z1 and Z2 being more similar to one another than Z3 (Fig. 2f). Most hepatocyte categories co-existed in different proportions across the PV-PV axis (H1, H2, H3), while hepatocytes in Z3, near to the CV, were predominantly from a single hepatocyte category (H5). An intermediate category (H4) also overlapped with categories H1-H3, but showed an enrichment towards the CV. Using Pittsburgh Heterogeneity Indices (e.g. Simpson's as a measure of Dominance; Shannon's as a measure of Heterogeneity) (35, 36) we evaluated the degree of hepatocyte structural diversity across the hepatic acinus. This analysis revealed increasing heterogeneity and decreasing hepatocyte category dominance from PV to middle regions of the acinus (Fig. 2f). In contrast, we observed a decrease heterogeneity and increase in hepatocyte category dominance near the CV consistent with the higher quantity of H5 in this region (Fig. 2e, f). In contrast to previous models of liver zonation (9-12), our results support a model in which zones in the liver are made up by combinations of structurally distinct populations of hepatocytes present in different proportions.

Interestingly, a recent proteomics analysis using single-cell Deep Visual Proteomics (scDVP) to study liver zonation also visualized five hepatocyte categories with distinct proteomes (24). However, the proportions of these categories and the degree of heterogeneity across the hepatic acinus were not measured. Therefore, to compare our scOrganellomic results with proteomic data, we applied the same spatial heterogeneity analysis to the clusters visualized by scDVP (Fig. 2f, g). Notably, proteomics-based Pittsburgh Heterogeneity plots mirrored our scOrganellomic findings. This also reveals that diverse hepatocyte populations with distinct proteomes reside within the zones of hepatic acini at different proportions (Fig. 2h). These results suggest organelle-signatures reflect the outcomes of proteomic adaptations that define hepatocyte diversity and functional specialization in different zones in the liver.

Nutritional perturbations shift organelle signatures and reduce hepatocyte heterogeneity in the liver.

To assess the functional relevance of the diverse organelle signatures and hepatocyte categories observed along the PV-CV axis, we studied how these adapted to changes in nutrient availability in the liver. To this end, we processed liver sections from control fed, fasted and western diet (WD) fed mice (37), revealing prominent changes in organelle features including size, number, and distribution along the PV–CV axis (Fig. 3a). Quantitative analysis using scOrganellomics confirmed important changes in the patterning of organelle features including, in some cases, reversed distribution along the PV-CV axis (e.g. mitochondria circularity and its distance to the nucleus) (Fig. 3b). Notably, while fasting conditions still retained some zonation patterns in organelle distribution, WD fed livers exhibited a loss of zonation, highlighting nutrition as a key driver of organelle adaptation (Fig. 3b, right panel).

We then examined the effect of different nutritional perturbations on hepatocyte heterogeneity, (Fig. 3c). Using PCA we visualized three distinct hepatocyte groups corresponding to each nutritional regiment. Interestingly, GMM clustering within each group showed reduced hepatocyte categories in fasted (4 clusters) and WD fed (3 clusters) animals compared to controls (5 clusters), yielding a total of 12 hepatocyte categories across all groups. Based on the observed segregation of hepatocyte clusters between different nutritional groups, we conclude that the reduction in hepatocyte categories in the experimental groups is not due to the loss of specific hepatocytes but rather a subcellular adaptation response leading to the acquisition of less diverse organelle signatures defining new hepatocyte categories. In line with an overall reduction in hepatocyte diversity under nutritional perturbations, we found a reduced heterogeneity of hepatocytes along the PV-CV axis of livers from both fasted and WD fed mice (Fig. 3d-g). This was particularly evident in WD fed mice, which exhibited fewer hepatocyte categories and greater dominance of specific categories (Fig. 3f, g).

We reveal that nutritional perturbations reduce hepatocyte heterogeneity by constraining organelle signature diversity. Moreover, these results highlight the power of our organelle-to-tissue scale analysis, suggesting a mechanism by which organelles adapt in response to nutrient availability to sustain the new cellular demands, which might in turn influence functional tissue plasticity.

Machine-Learning assisted scOrganellomics Predicts Hepatic Heterogeneity, Nutritional Status, and Disease Progression.

Based on our results using different nutritional regiments, we reasoned organelle signatures could link subcellular architecture to specific metabolic states and could be implemented to predict organelle adaptation in response to changes in nutritional input.

To evaluate whether organelle signatures have enough information to predict hepatic heterogeneity and nutritional states, we developed Multilayer Perceptron (MLP) machine learning models using all ~100 organelle metrics as predictors (Fig. 4a). We randomized our data sets and used 80% of images from all experimental groups for training and 20% for validation. Our models displayed high accuracy predicting between the nutritional status of mice (average accuracy = 99.4, Fig. 4b) and distinguishing between all 12 hepatocyte categories (average accuracy = 94.8, Fig. 4c). These results highlight the power of organelle signatures as “structural fingerprints” defining not only cellular heterogeneity within complex tissues but also helping identify the animal's nutritional condition.

Encouraged by these results we tested whether our machine-learning assisted scOrganellomics strategy was sufficient to predict changes in subcellular architecture in response to metabolic disease progression. As model of early stages of MASLD, male mice were fed with WD for up to 50 days, and liver samples were collected at different intervals (0, 7, 17, 31, 42, and 50 days). Early signs of steatosis, such as lipid accumulation accompanied by mitochondrial and peroxisomal morphological changes, were observed by day 7, with progressively severe alterations of tissue architecture and lipid droplet accumulation over time (38). By later time points, organelle architecture showed advanced features of MASLD, including disrupted zonation patterns, cell ballooning, enlarged lipid droplets, extensive mitochondrial fragmentation and peroxisomal aggregation (Fig. 4d) (39). Using this new dataset, we trained an MLP model of liver disease progression that reached about 80% accuracy predicting between different MASLD stages (Fig. 4d, e). These findings underscore the proficiency of organelle signatures as powerful indicators to

monitor disease progression and suggest a broader application of this approach to understand tissue-level pathological changes, particularly in the later stages of metabolic diseases.

Discussion

Understanding how the liver adapts to different nutritional challenges is central to physiology, yet it has been challenging to study at the cellular and subcellular level in vivo. Advances in single-cell transcriptomics have shown different hepatocyte subtypes in control conditions but they require tissue dissociation, losing the spatial context in vivo (21-23). Further, spatial proteomics revealed different hepatocyte subtypes across liver zones (24). However, this strategy remains low throughput and thus limited to assess changes in hepatocyte adaptation under different experimental conditions. Here, combining imaging-based scOrganellomics and machine learning strategies, we demonstrate that organelle signatures define the functional heterogeneity of hepatocytes across liver zones, revealing adaptations to different nutritional challenges. Importantly, this strategy allowed us to predict the functional status of the liver at the single-cell level, both in physiological conditions and in an early model of MASLD disease.

We demonstrate that hepatocytes are zonated based on their organelle signatures in situ. However, in contrast to previous models (9-12), we discover that structurally distinct hepatocytes co-exist within liver zones. We confirmed this heterogeneity is also present in spatial proteomic datasets but was previously overlooked (24). Further, this hepatocyte heterogeneity is highly reduced under different nutritional challenges, including high-fat/high-carbohydrate diet, and fasting. This finding suggests that single-cell variation within liver zones could be relevant to maintain proper tissue function (28, 40). One possibility is that hepatocytes within a given zone receive different concentrations of nutrients and gases due to differences in polarity towards smaller vessels. Future studies using higher resolution imaging, such as volumetric EM or Expansion Microscopy (41-43) could help to solve this question.

The machine learning strategy presented in this study not only allows to classify hepatocytes based on subcellular architecture, but also to make predictions about their cellular status based exclusively on organelle signatures. In addition to accurately predicting the nutritional status and hepatocyte category under physiological conditions, this pipeline successfully predicted the status of the liver across six different time points of MASLD disease. Further additions to the machine learning pipeline could allow to distinguish the specific organelle changes underlying metabolic and disease conditions to guide modeling of the disease as a powerful hypothesis generating engine.

Several improvements to the present strategy could be implemented in the future. Currently, scOrganellomics and machine learning allowed us to distinguish 5 hepatocyte clusters in vivo. Further expanding the number of organelles and their analyzed features could reveal new functional hepatocyte classes important for liver function. Moreover, our current resolution limits the analysis of inter-organelle contacts, which could further reveal how different hepatocyte categories perform differential functions across liver zones. Future studies including large volumetric EM datasets or Expansion microscopy of entire liver acini would allow to include the organelle contacts as part of this analysis pipeline. Moreover, in the present study we combine a transgenic mouse line which labels all mitochondria (mtDendra2) with different dyes and

antibodies for other subcellular structures including peroxisomes and lipid droplets. However, it would be helpful to develop a transgenic line combining multiple organelle markers to apply our current analysis strategy to physiological and disease conditions in a living organism.

In conclusion, we present a spatially resolved organelle signature-based toolbox for the characterization and prediction of cellular status in tissues. While we applied this strategy to study the mouse liver, we envision that this strategy could be extended to other tissues and species of interest. This new method overcomes previous limitations including low throughput and high cost of some spatial proteomic strategies as it relies in standard histological processing of samples and allows automatized analysis of thousands of cells and experimental conditions. scOrganellomics in combination with other spatially resolved omics techniques, could not only help us understand the mechanisms of cellular adaptation to physiological challenges but could help determine fundamental relationships between proteins and subcellular changes underlying the progression of a disease. We foresee that this pipeline could also be applied to assess the status of human livers under different disease conditions. Such strategy, based exclusively on organelle profiling, could transform disease modeling and advance strategies for personalized therapy.

References

1. Carter B, Zhao K. The epigenetic basis of cellular heterogeneity. Nat Rev Genet. 2021 Apr;22(4):235-250. doi: 10.1038/s41576-020-00300-0. Epub 2020 Nov 26. PMID: 33244170; PMCID: PMC10880028.

2. Gupta RK, Kuznicki J. Biological and Medical Importance of Cellular Heterogeneity Deciphered by Single-Cell RNA Sequencing. Cells. 2020 Jul 22;9(8):1751. doi: 10.3390/cells9081751. PMID: 32707839; PMCID: PMC7463515.

3. Alberts B, Johnson A, Lewis J, et al. New York: Garland Science; 2002.

4. Bar-Peled L, Kory N. Principles and functions of metabolic compartmentalization. Nat Metab. 2022 Oct;4(10):1232-1244. doi: 10.1038/s42255-022-00645-2. Epub 2022 Oct 20. PMID: 36266543; PMCID: PMC10155461.

5. Ben-Moshe S, Itzkovitz S. Spatial heterogeneity in the mammalian liver. Nat Rev Gastroenterol Hepatol. 2019 Jul;16(7):395-410. doi: 10.1038/s41575-019-0134-x. PMID: 30936469.

6. Sukumaran A, Choi K, Dasgupta B. Insight on Transcriptional Regulation of the Energy Sensing AMPK and Biosynthetic mTOR Pathway Genes. Front Cell Dev Biol. 2020 Jul 29;8:671. doi: 10.3389/fcell.2020.00671.

7. Atger, F., Gobet, C., Marquis, J., Martin, E., Wang, J., Weger, B., et al. (2015). Circadian and feeding rhythms differentially affect rhythmic mRNA transcription and translation in mouse liver. Proc. Natl. Acad. Sci. U.S.A. 112, E6579–E6588.

8. Fast EM, Sporrij A, Manning M, Rocha EL, Yang S, Zhou Y, Guo J, Baryawno N, Barkas N, Scadden D, Camargo F, Zon LI. External signals regulate continuous transcriptional states in hematopoietic stem cells. Elife. 2021 Dec 23;10:e66512. doi: 10.7554/eLife.66512. PMID: 34939923; PMCID: PMC8700284.

9. Cunningham RP, Porat-Shliom N. Liver Zonation - Revisiting Old Questions With New Technologies. Front Physiol. 2021 Sep 9;12:732929. doi: 10.3389/fphys.2021.732929. PMID: 34566696; PMCID: PMC8458816.

10. Noël, R. (1923). Recherches Histo-Physiologiques sur la Cellule Hépatique des Mammifères. Paris: University of Paris.

11. Jungermann, K., and Kietzmann, T. (1996). Zonation of parenchymal and nonparenchymal metabolism in liver. Annu. Rev. Nutr. 16, 179–203. doi: 10.1146/annurev.nu.16.070196.001143

12. Ben-Moshe, S., and Itzkovitz, S. (2019). Spatial heterogeneity in the mammalian liver. Nat. Rev. Gastroenterol. Hepatol. 16, 395–410. doi: 10.1038/s41575-019-0134-x

13. Schulze RJ, Schott MB, Casey CA, Tuma PL, McNiven MA. The cell biology of the hepatocyte: A membrane trafficking machine. J Cell Biol. 2019 Jul 1;218(7):2096-2112. doi: 10.1083/jcb.201903090. Epub 2019 Jun 14. PMID: 31201265; PMCID: PMC6605791.

14. Heald R, Cohen-Fix O. Morphology and function of membrane-bound organelles. Curr Opin Cell Biol. 2014 Feb;26:79-86. doi: 10.1016/j.ceb.2013.10.006. Epub 2013 Nov 16. PMID: 24529249; PMCID: PMC3927147.

15. Cho NH, Cheveralls KC, Brunner AD, Kim K, Michaelis AC, Raghavan P, Kobayashi H, Savy L, Li JY, Canaj H, Kim JYS, Stewart EM, Gnann C, McCarthy F, Cabrera JP, Brunetti RM, Chhun BB, Dingle G, Hein MY, Huang B, Mehta SB, Weissman JS, Gómez-Sjöberg R, Itzhak DN, Royer LA, Mann M, Leonetti MD. OpenCell: Endogenous tagging for the cartography of human cellular organization. Science. 2022 Mar 11;375(6585):eabi6983. doi: 10.1126/science.abi6983. Epub 2022 Mar 11. PMID: 35271311; PMCID: PMC9119736.

16. Valm AM, Cohen S, Legant WR, Melunis J, Hershberg U, Wait E, Cohen AR, Davidson MW, Betzig E, Lippincott-Schwartz J. Applying systems-level spectral imaging and analysis to reveal the organelle interactome. Nature. 2017 Jun 1;546(7656):162-167. doi: 10.1038/nature22369. Epub 2017 May 24. PMID: 28538724; PMCID: PMC5536967.

17. Loud AV. A quantitative stereological description of the ultrastructure of normal rat liver parenchymal cells. J Cell Biol. 1968 Apr;37(1):27-46. doi: 10.1083/jcb.37.1.27.

18. Jacobi D, Liu S, Burkewitz K, Kory N, Knudsen NH, Alexander RK, Unluturk U, Li X, Kong X, Hyde AL, Gangl MR, Mair WB, Lee CH. Hepatic Bmal1 Regulates Rhythmic Mitochondrial Dynamics and Promotes Metabolic Fitness. Cell Metab. 2015 Oct 6;22(4):709-20. doi: 10.1016/j.cmet.2015.08.006.

19. Gordaliza-Alaguero I, Cantó C, Zorzano A. Metabolic implications of organelle-mitochondria communication. EMBO Rep. 2019 Sep;20(9):e47928. doi: 10.15252/embr.201947928.

20. Seymour CA, Peters TJ. Changes in hepatic enzymes and organelles in alcoholic liver disease. Clin Sci Mol Med. 1978 Oct;55(4):383-9. doi: 10.1042/cs0550383.

21. Bahar Halpern, K. et al. Single-cell spatial reconstruction reveals global division of labour in the mammalian liver. *Nature* **542**, 352–356 (2017).

22. Su Q, Kim SY, Adewale F, Zhou Y, Aldler C, Ni M, Wei Y, Burczynski ME, Atwal GS, Sleeman MW, Murphy AJ, Xin Y, Cheng X. Single-cell RNA transcriptome landscape of hepatocytes and non-parenchymal cells in healthy and NAFLD mouse liver. iScience. 2021 Oct 6;24(11):103233. doi: 10.1016/j.isci.2021.103233. PMID: 34755088; PMCID: PMC8560975.

23. Aizarani N, Saviano A, Sagar, Mailly L, Durand S, Herman JS, Pessaux P, Baumert TF, Grün D. A human liver cell atlas reveals heterogeneity and epithelial progenitors. Nature. 2019 Aug;572(7768):199-204. doi: 10.1038/s41586-019-1373-2. Epub 2019 Jul 10. PMID: 31292543; PMCID: PMC6687507.

24. Rosenberger FA, Thielert M, Strauss MT, Schweizer L, Ammar C, Mädler SC, Metousis A, Skowronek P, Wahle M, Madden K, Gote-Schniering J, Semenova A, Schiller HB, Rodriguez E, Nordmann TM, Mund A, Mann M. Spatial single-cell mass spectrometry defines zonation of the hepatocyte proteome. Nat Methods. 2023 Oct;20(10):1530-1536. doi: 10.1038/s41592-023-02007-6. Epub 2023 Oct 2. PMID: 37783884; PMCID: PMC10555842.

25. Another in vitro machine learning analysis of organelle structure in addition to Sarah's paper?

26. Silva BSC, DiGiovanni L, Kumar R, Carmichael RE, Kim PK, Schrader M. Maintaining social contacts: The physiological relevance of organelle interactions. Biochim Biophys Acta Mol Cell Res. 2020 Nov;1867(11):118800. doi: 10.1016/j.bbamcr.2020.118800. Epub 2020 Jul 23. PMID: 32712071; PMCID: PMC7377706.

27. Graziani V, Crosas-Molist E, George SL, Sanz-Moreno V. Organelle adaptations in response to mechanical forces during tumour dissemination. Curr Opin Cell Biol. 2024 Jun;88:102345. doi: 10.1016/j.ceb.2024.102345. Epub 2024 Mar 12. PMID: 38479111.

28. Eberwine J, Kim J, Anafi RC, Brem S, Bucan M, Fisher SA, Grady MS, Herr AE, Issadore D, Jeong H, Kim H, Lee D, Rubakhin S, Sul JY, Sweedler JV, Wolf JA, Zaret KS, Zou J. Subcellular omics: a new frontier pushing the limits of resolution, complexity and throughput. Nat Methods. 2023 Mar;20(3):331-335. doi: 10.1038/s41592-023-01788-0. PMID: 36899160; PMCID: PMC10049458.

29. Lodhi IJ, Semenkovich CF. Peroxisomes: a nexus for lipid metabolism and cellular signaling. Cell Metab. 2014 Mar 4;19(3):380-92. doi: 10.1016/j.cmet.2014.01.002. Epub 2014 Feb 6. PMID: 24508507; PMCID: PMC3951609.

30. Najt CP, Adhikari S, Heden TD, Cui W, Gansemer ER, Rauckhorst AJ, Markowski TW, Higgins L, Kerr EW, Boyum MD, Alvarez J, Brunko S, Mehra D, Puchner EM, Taylor EB, Mashek DG. Organelle interactions compartmentalize hepatic fatty acid trafficking and metabolism. Cell Rep. 2023 May 30;42(5):112435. doi: 10.1016/j.celrep.2023.112435. Epub 2023 Apr 26. PMID: 37104088; PMCID: PMC10278152.

31. Ma R, Martínez-Ramírez AS, Borders TL, Gao F, Sosa-Pineda B. Metabolic and non-metabolic liver zonation is established non-synchronously and requires sinusoidal Wnts. Elife. 2020 Mar 10;9:e46206. doi: 10.7554/eLife.46206. PMID: 32154783; PMCID: PMC7067564.

32. Ben-Moshe S, Shapira Y, Moor AE, Manco R, Veg T, Bahar Halpern K, Itzkovitz S. Spatial sorting enables comprehensive characterization of liver zonation. Nat Metab. 2019 Sep;1(9):899-911. doi: 10.1038/s42255-019-0109-9. Epub 2019 Sep 16. PMID: 31535084; PMCID: PMC6751089.

33. Fransen M, Lismont C, Walton P. The Peroxisome-Mitochondria Connection: How and Why? Int J Mol Sci. 2017 May 24;18(6):1126. doi: 10.3390/ijms18061126. PMID: 28538669; PMCID: PMC5485950.

34. Pham AH, McCaffery JM, Chan DC. Mouse lines with photo-activatable mitochondria to study mitochondrial dynamics. Genesis. 2012 Nov;50(11):833-43. doi: 10.1002/dvg.22050. Epub 2012 Aug 11. PMID: 22821887; PMCID: PMC3508687.

35. Gough, A.; Shun, T. Y.; Lansing Taylor, D.; et al. A Metric and Workflow for Quality Control in the Analysis of Heterogeneity in Phenotypic Profiles and Screens. Methods 2016, 96, 12–26.

36. Gough, A. H.; Chen, N.; Shun, T. Y.; et al. Identifying and Quantifying Heterogeneity in High Content Analysis: Application of Heterogeneity Indices to Drug Discovery. PLoS One 2014, 9, e102678.

37. Ghallab A, Myllys M, Friebel A, Duda J, Edlund K, Halilbasic E, Vucur M, Hobloss Z, Brackhagen L, Begher-Tibbe B, Hassan R, Burke M, Genc E, Frohwein LJ, Hofmann U, Holland CH, González D, Keller M, Seddek AL, Abbas T, Mohammed ESI, Teufel A, Itzel T, Metzler S, Marchan R, Cadenas C, Watzl C, Nitsche MA, Kappenberg F, Luedde T, Longerich T, Rahnenführer J, Hoehme S, Trauner M, Hengstler JG. Spatio-Temporal Multiscale Analysis of Western Diet-Fed Mice Reveals a Translationally Relevant Sequence of Events during NAFLD Progression. Cells. 2021 Sep 23;10(10):2516. doi: 10.3390/cells10102516. PMID: 34685496; PMCID: PMC8533774.

38. Fang T, Wang H, Pan X, Little PJ, Xu S, Weng J. Mouse models of nonalcoholic fatty liver disease (NAFLD): pathomechanisms and pharmacotherapies. Int J Biol Sci. 2022 Sep 6;18(15):5681-5697. doi: 10.7150/ijbs.65044. PMID: 36263163; PMCID: PMC9576517.

39. Soto A, Spongberg C, Martinino A, Giovinazzo F. Exploring the Multifaceted Landscape of MASLD: A Comprehensive Synthesis of Recent Studies, from Pathophysiology to Organoids and

Beyond. Biomedicines. 2024 Feb 8;12(2):397. doi: 10.3390/biomedicines12020397. PMID: 38397999; PMCID: PMC10886580.

40. Dueck H, Eberwine J, Kim J. Variation is function: Are single cell differences functionally important?: Testing the hypothesis that single cell variation is required for aggregate function. Bioessays. 2016 Feb;38(2):172-80. doi: 10.1002/bies.201500124. Epub 2015 Dec 2. PMID: 26625861; PMCID: PMC4738397.

41. Knott G, Marchman H, Wall D, Lich B. Serial section scanning electron microscopy of adult brain tissue using focused ion beam milling. J Neurosci. 2008 Mar 19;28(12):2959-64. doi: 10.1523/JNEUROSCI.3189-07.2008. PMID: 18353998; PMCID: PMC6670719.

42. C Shan Xu Kenneth J Hayworth Zhiyuan Lu Patricia Grob Ahmed M Hassan José G García-Cerdán Krishna K Niyogi Eva Nogales Richard J Weinberg Harald F Hess (2017) Enhanced FIB-SEM systems for large-volume 3D imaging eLife 6:e25916.

43. Wang Y, Eddison M, Fleishman G, Weigert M, Xu S, Wang T, Rokicki K, Goina C, Henry FE, Lemire AL, Schmidt U, Yang H, Svoboda K, Myers EW, Saalfeld S, Korff W, Sternson SM, Tillberg PW. EASI-FISH for thick tissue defines lateral hypothalamus spatio-molecular organization. Cell. 2021 Dec 22;184(26):6361-6377.e24. doi: 10.1016/j.cell.2021.11.024. Epub 2021 Dec 6. PMID: 34875226

Figure legends

Fig. 1 Tissue-to-organelle analysis pipeline integrates microscopy and machine learning to reveal spatial organelle adaptations in the liver lobule. (**a**) Schematic of the liver lobule illustrating the spatial gradients of nutrients, gases, and hormones between the portal vein (PV) and central vein (CV). Hepatocyte responses to these gradients are hypothesized to be encoded within the subcellular organelle architecture, supporting metabolic liver zonation. (**b**) Overview of the tissue-to-organelle analysis pipeline. Confocal microscopy images of fixed liver slices, with fluorescent labeling of cell boundaries, mitochondria, peroxisomes, and lipid droplets, were processed using the custom Liv_Zones software package. The pipeline enables segmentation of cells and organelles, followed by quantitative feature extraction. The lower panel highlights successful segmentation of cells at tissue level and organelles at single cell level. (**c**) Microscopic imaging of liver lobules demonstrating functional zonation (left panel) via markers Aldolase B (enriched near PV) and CYP2E1 (enriched near CV). These markers delineate three concentric zones: zone 1, zone 2, and zone 3. The image reveals the lobular structure, with a CV surrounded by six PVs, and demonstrates the capacity for large-area visualization via confocal microscopy. The left panel shows functional zonation in the acinus, while the right panel displays organelle heterogeneity across liver zones in control fed mice. Insets from the acinus highlight high-resolution visualization of organelle features. (**d**) Heatmap of spatial organelle feature distribution along the PV-to-CV axis. The x-axis represents relative cell positions within the lobule, while the y-axis lists individual organelle features. Normalized z-scores (color scale: white for -1 to purple for +1) reveal spatial variations in organelle architecture, emphasizing the heterogeneity of subcellular structures across the lobular axis.

Fig. 2 Organelle signatures reveal hepatocyte spatial heterogeneity in the liver acinus, comparable to proteomics. (**a**) Volcano plot illustrating differences in organelle features

between three functional zones in the liver. Each point represents a single organelle feature, with the x-axis showing the log2 fold change (logFC) between regions and the y-axis displaying the -log10 of the False Discovery Rate (FDR). Organelles with significant differences (FDR < 0.05) are shown as larger circles, with those enriched in one region colored purple and those enriched in the other region colored blue. The pie chart above the plot indicates the relative contribution of each organelle to defining primary differences between the liver zones. (**b**) Principal component analysis (PCA) plot of five distinct hepatocyte categories (H1-H5) derived from over 3000 hepatocytes in control mice, identified using a Gaussian Mixture Models (GMM). (**c**) Heatmap showing unique clustering patterns between hepatocyte categories based on mitochondrial, peroxisomal, and lipid droplet properties. The color scale represents normalized z-scores, ranging from -1 (black, indicating lower-than-average values) to +1 (white, indicating higher-than-average values), highlighting variations in organelle signatures across hepatocyte categories. (**d**) Bar graphs depicting the proportion of organelle subtypes within each hepatocyte category. Organelle subtypes were defined by area (see supplementary materials). The x-axis represents the percentage of each organelle subtype, while the y-axis represents the hepatocyte categories. The colors in the bars correspond to the subtype of each organelle as indicated below the graphs. (**e**) PCA plot demonstrating the distribution of hepatocyte categories within the acinus. Each dot represents a hepatocyte, with color indicating the relative position within the acinus, from the portal vein (white) to the central vein (purple). Histograms show the frequency of each hepatocyte category from the portal vein (PV) to the central vein (CV). (**f**) Histogram of the proportion of each hepatocyte category identified by organelle-based clustering (left) across the three liver zones. The histogram in the middle shows Pittsburgh Heterogeneity indices, including Simpson's index (for dominance) and Shannon's entropy (for heterogeneity), based on organelle-based clustering along the PV-to-CV axis. (**g**) PCA plot of previous proteomics dataset (24) identifying five hepatocyte categories using a Gaussian Mixture Models (GMM). The histogram in the middle shows the proportion of each hepatocyte category based on proteomics clustering, and the histogram on the left shows Pittsburgh Heterogeneity indices for Simpson's index and Shannon's entropy, based on proteomics clustering along the PV-to-CV axis.

Fig. 3 Changes in nutritional inputs reduce organelle-based hepatocyte heterogeneity. (**a**) Microscopic images of liver acinus (from portal vein (PV) to central vein (CV)) from control fed, overnight-fasted, and western diet (WD) fed mice. Animals were fed with a control diet for 10 weeks, with livers harvested (control), or overnight-fasted before liver collection (fasting), or replaced with a WD diet at week 6 until liver collection at 10 weeks (WD). Images were acquired after fluorescent labeling of cell boundaries and organelles. Insets below each image show magnified areas from the PV and CV regions for visual comparison of architectural changes among the three organelles. (**b**) Heatmaps showing the distribution of organelle features (mitochondria, peroxisomes, and lipid droplets) in the control, fasting, and WD groups. The x-axis corresponds to the relative cell position within acinus, spanning from PV to CV, and the y-axis displays selected organelle features. The color scale represents normalized z-scores, ranging from -1 (white, indicating lower-than-average values) to +1 (purple, indicating higher-than-average values), highlighting the spatial distribution of organelle architecture. (**c**) Principal component analysis (PCA) plot depicting three distinct hepatocyte clusters from the control, fasting, and WD groups. Hepatocytes (~7000) from all experimental groups were subjected to clustering based on organelle signatures using a Gaussian Mixture Models (GMM) and PCA. Three distinct colors represent hepatocytes from each experimental group, as indicated. Small PCA plots on the left and right show hepatocyte categories based on organelle signatures within the fasting and WD groups, respectively, with the distribution of these categories along the PV-to-CV axis shown above. (**d**) Acinus illustrating the distribution of hepatocyte categories from control (**e**), fasting (**f**), and WD (g) groups. Hepatocytes from each experimental group were plotted within the acinus based on their positional information. The different colors represent

distinct hepatocyte categories as indicated. The plot on the left shows the proportion of each hepatocyte category within the respective experimental group along the PV-to-CV axis. (**g**) Line charts showing Pittsburgh Heterogeneity indices: Simpson's index (for dominance) (left chart) and Shannon's Entropy (for heterogeneity) (right chart) of overall hepatocyte categories. The three continuous lines represent each experimental group, as indicated. The x-axis represents distance from PV to CV with 100 bins, while the y-axis shows the respective value of the index. The line charts below Pittsburgh Heterogeneity indices plot represent the percentage change in dominance (left) and diversity (right) compared to control along the PV-to-CV length, also binned into 100.

Fig. 4 Organelle signatures assist machine learning to predict cellular states. (**a**) Schematic representation showing the process to generate a multilayer perceptron (MLP) model for predicting cellular states using organelle signatures. The model is trained on single-cell organelle signatures as inputs, which are processed through four hidden layers, each containing 32 neurons. A total of 80% of the complete acini (containing all hepatocytes within the acinus) from each experimental group were used for training, with the remaining 20% used for validation. Three models were developed to predict nutritional regimen, hepatocyte categories, and disease progression. (**b**) Validation of the custom MLP model to predict nutritional regimen. The numbers in the validation matrix represent the percentage of times the model correctly predicts the nutritional regimen. (**c**) Validation of the custom MLP model to predict hepatocyte categories from all three nutritional groups. The numbers in the validation matrix represent the percentage of times the model correctly predicts the hepatocyte category. (**d**) Microscopic images of liver acinus (from portal vein (PV) to central vein (CV)) from western diet (WD) fed mice. Six-week-old male mice were fed with a western diet for varying days, such that livers were harvested at the same age. Images were acquired after fluorescent labeling of cell boundaries and organelles. Six images from top to bottom correspond to 0, 7, 17, 41, 40, and 50 days of WD feeding. (**e**) Validation of the custom MLP model to predict liver disease progression. The numbers in the validation matrix represent the percentage of times the model correctly predicts the hepatocyte category.

Material and Methods

Animal Experiments

Eight-week-old Pham^{Excised} C57BL/6J (strain #018397) mice carrying the Mito-Dendra2 transgene (heterozygous males and females) were obtained from Jackson Laboratories. Breeding between heterozygous males and females was performed to obtain homozygous males. Homozygous males were then crossed with C57BL/6J wild-type females to generate heterozygous progeny for experimental use. Breeding was conducted in the vivarium at Janelia Research Campus.

For nutritional perturbation experiments, all animals were maintained on a control diet (TestDiets 58B0) up to 6 weeks of age. Control (n=4) and overnight-fasted groups (n=4) continued this diet until 10 weeks. In the overnight-fasted group, food was removed at 6 pm the day before sacrifice. The Western diet (WD) group (n=3) received a high-fat diet (TestDiets 5GDD) starting at 6 weeks of age and continued until 10 weeks. Only male mice were used in this study.

For MASLD progression experiments, animals were placed on a high-fat diet starting as early as 6 weeks of age. Liver samples were collected at 7, 17, 31, 40, and 50 days of WD feeding (n=2 for each time point), corresponding to time points retrospectively calculated to align the final age of all animals during excision.

Livers were harvested at 6 am via cardiac perfusion with 1x PBS to clear blood, followed by perfusion with 30 ml of 4% paraformaldehyde (PFA) at a controlled rate of 2.5 ml/min to prevent endothelial disruption. Harvested livers were immersed in 4% PFA for 24 hours, washed three times with 1x PBS, and stored in 1% PFA until immunostaining.

Animal care followed NIH guidelines and was approved by the Institutional Animal Care and Use Committee (Protocol #22-0229.04) at Janelia Research Campus, Howard Hughes Medical Institute. Mice were housed under a 12-hour light/dark cycle in temperature- and humidity-controlled, sound-attenuated rooms with ad libitum access to food and water.

Immunostaining and Image Acquisition

Liver samples were embedded in 4.6% low-melting-point agarose and sectioned into 120 µm slices using a Leica Vibratome (LEICA VT 1200S). Sections were blocked for 1 hour in blocking buffer (10% FBS + 0.5% Triton X-100 in PBS) and incubated with primary antibodies in the same buffer for 48 hours at 4°C. Mouse anti-PMP70 (MilliporeSigma, SAB4200181, 1:75) was used to label peroxisomes. Secondary staining was performed overnight at 4°C using Alexa Fluor goat anti-mouse antibody (Thermo Fisher, A21235, 1:500). Alexa Fluor Plus 555 Phalloidin (Thermo Fisher, A30106, 1:100) and HCS LipidTox Red (Thermo Fisher, H34476, 1:100) were used to label cell boundaries and lipid droplets, respectively. Tissue clearing was performed using EasyIndex (Life Canvas Technologies, EI-500-1.52): sections were incubated in 50% EasyIndex for 1 hour, followed by 100% EasyIndex for 3–5 hours. Cleared sections were mounted on glass slides using Secure-Seal Space (Thermo Fisher, 0523073).

Images were acquired with a Leica Stellaris 8 confocal microscope. For each liver section, at least three lobules were selected, and three acini per lobule (spanning the PV to CV axis) were imaged to a depth of 10 µm (50 z-sections per acquisition).

Developing Organelle Segmentation Models

Organelle segmentation models were developed using Cellpose v2 with a supervised, human-in-the-loop annotation. For model training, 35 random 2D image crops (spanning PV to CV) containing at least 10 cells per crop were selected from each nutritional group. Separate models were trained for hepatocytes, mitochondria, lipid droplets, and peroxisomes to ensure robust segmentation across experimental conditions.

Image Processing and Data Analysis

Images were processed using the Liv-Zones pipeline. Portal and central veins were manually annotated, and acini were cropped to 1.2 × 0.4 of the PV-CV distance. Ten z-slices were stacked to enhance organelle visibility, resulting in five stacks per acinus. Using custom Cellpose models, hepatocytes and organelles were segmented in 2D across all z-stacks. Features of mitochondria, lipid droplets, and peroxisomes were extracted using skimage.regionprops and aggregated at the single-cell level. Due to the wide range of lipid droplet sizes, segmentation was performed three times with diameter parameters of 16, 132, and 645. Cells were linked across z-stacks using Motile (https://github.com/funkelab/motile), and their features were averaged for downstream analysis.

Organelle features across PV to CV regions were analyzed for deviations from control distributions. Metrics such as hepatocyte diversity and dominance indices were computed using the Pittsburgh Heterogeneity Index. Gaussian mixture models (GMM) and Principal component

analysis (PCA) were employed for clustering hepatocytes based on organelle features. Visualization of organelle features within acinus is done by custom scripts based on python packages.

For machine learning analysis, a multilayer perceptron (MLP) with 4 hidden layers (32 neurons each) was trained on 16 single cell features to predict hepatocyte categories, nutritional regimen, and disease progression. The model was trained on cells from 80% the complete acini associated with all the experimental groups while remaining 20% was used for validation, achieving over 80% accuracy in classifying nutritional and disease states.

Code Availability

Liv_Zones pipeline with hepatocyte and organelle segmentation models is available at GitHub - ahillsley/liv_zones, while the Motile tool for cell linking can be found at https://github.com/funkelab/motile

Acknowledgments

We thank the Janelia Shared resources for their excellent technical support. We thank Wyatt Korff and Ron Vale for their feedback during the development of this project. We thank Triveni Menon for revision of this manuscript, and Joaquin Lilao-Garzón for critical feedback about the experiments. We thank Alison Howard and Victoria Custard for administrative support.
Funding: This work was supported by Howard Hughes Medical Institute.

Author contributions

Conceptualization: D.F. methodology: D.F., R.A., A.D.J; investigation: D.F., R.A, A.D.J; machine learning workflow development and analysis: D.F., A.H., J.F., writing, review and editing: D.F., I.E.-M and R.A; visualization: D.F., R.A., supervision: D.F., J.F., project administration, D.F., J.F.; funding acquisition, D.F., J.F.

Declaration of interests

The authors declare no competing interests.

Figure 1.

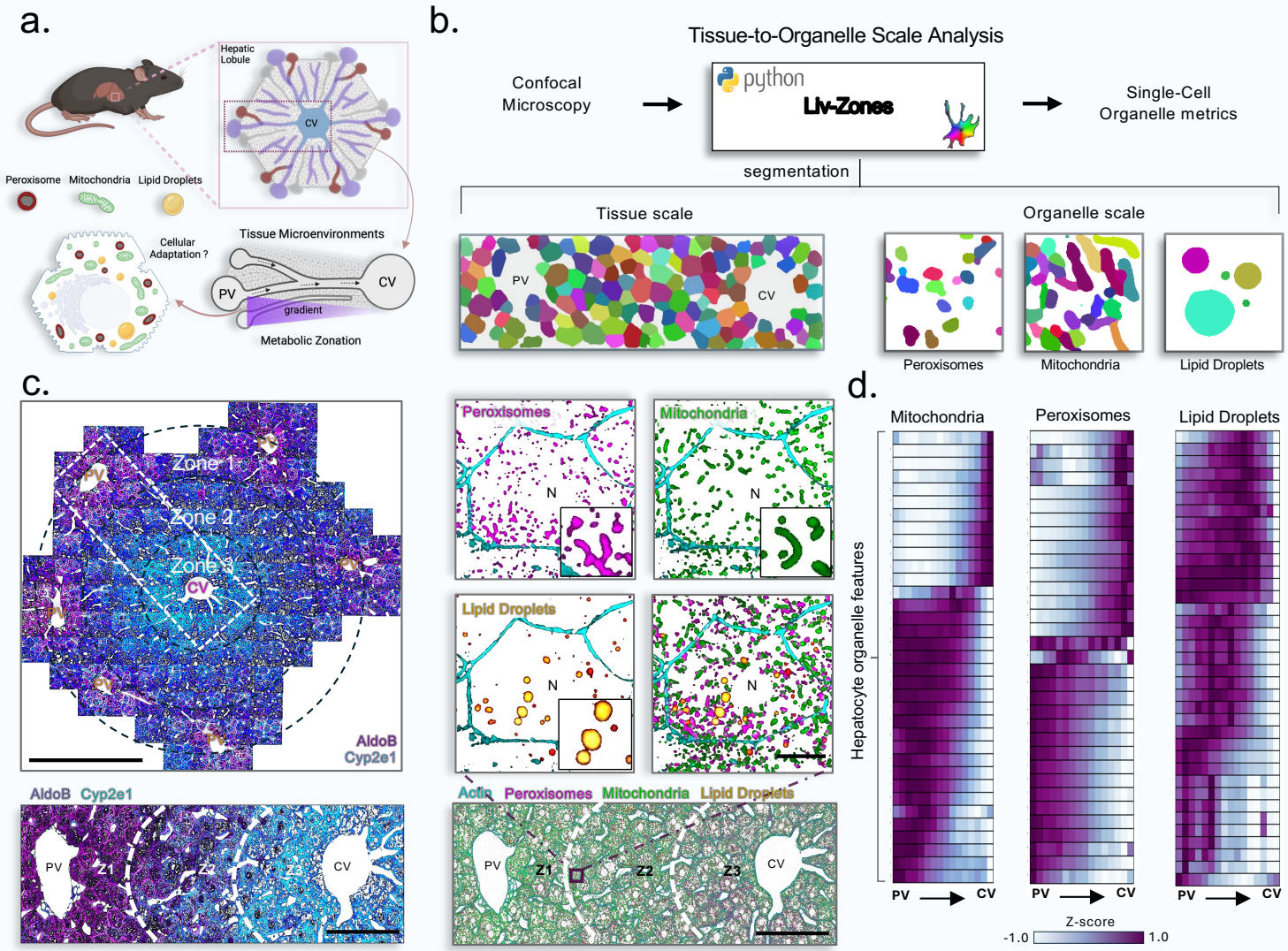
a.
Hepatic Lobule
CV
Peroxisome
Mitochondria
Lipid Droplets
Cellular Adaptation ?
Tissue Microenvironments
PV
CV
gradient
Metabolic Zonation
b.
Tissue-to-Organelle Scale Analysis
Confocal Microscopy
python
Liv-Zones
Single-Cell Organelle metrics
segmentation
Tissue scale
Organelle scale
PV
CV
Peroxisomes
Mitochondria
Lipid Droplets
N
Actin
c.
Zone 1
Zone 2
Zone 3
AldoB
Cyp2e1
Z1
Z2
Z3
d.
Mitochondria
Peroxisomes
Lipid Droplets
Hepatocyte organelle features
Z-score
-1.0
1.0

Figure 2.

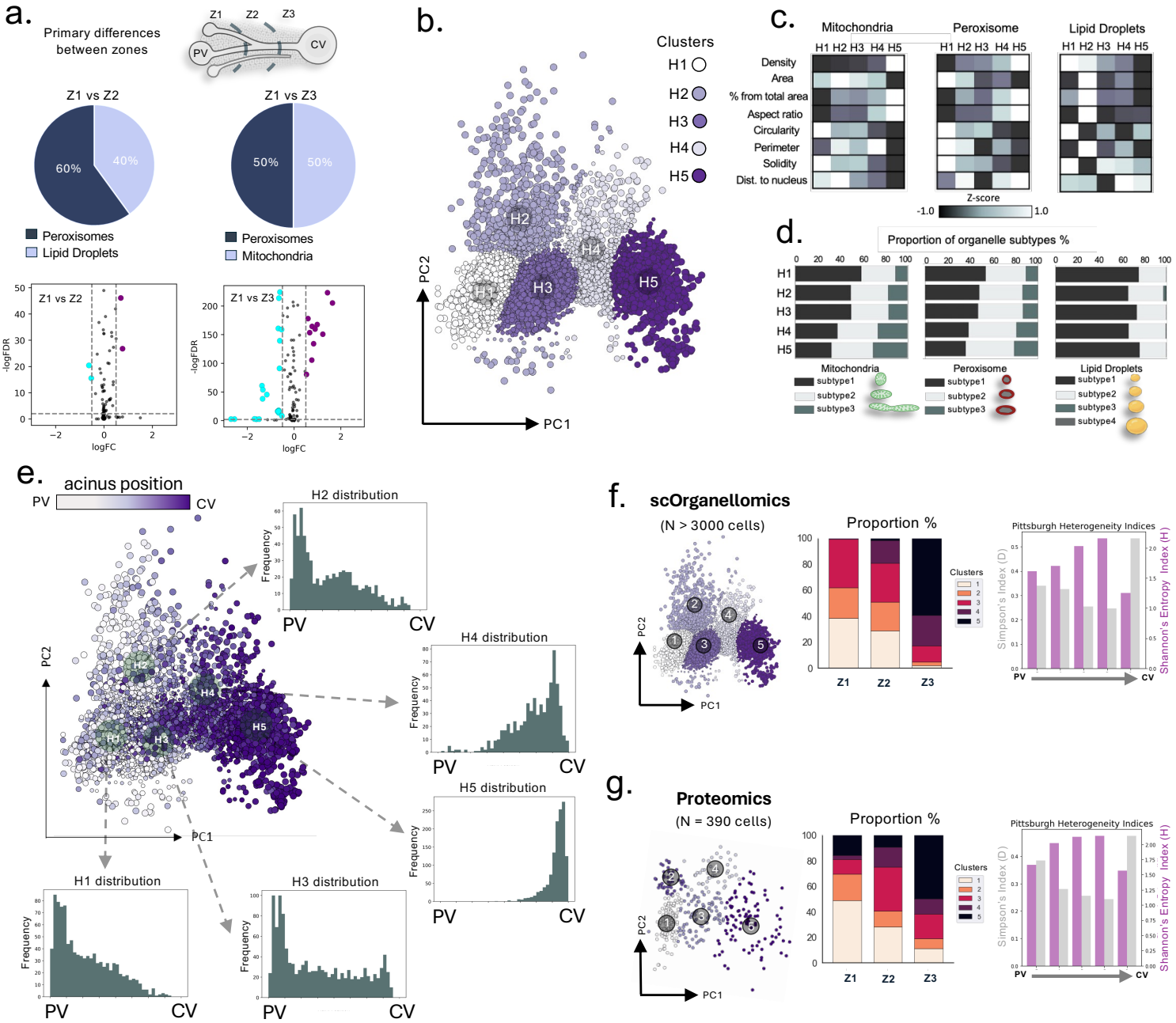
a.
Primary differences between zones
Z1
Z2
Z3
PV
CV
Z1 vs Z2
60%
40%
Peroxisomes
Lipid Droplets
Z1 vs Z3
50%
50%
Peroxisomes
Mitochondria
Z1 vs Z2
Z1 vs Z3
-logFDR
logFC
b.
Clusters
H1
H2
H3
H4
H5
PC2
PC1
c.
Mitochondria
Peroxisome
Lipid Droplets
H1 H2 H3 H4 H5
Density
Area
% from total area
Aspect ratio
Circularity
Perimeter
Solidity
Dist. to nucleus
Z-score
-1.0
1.0
d.
Proportion of organelle subtypes %
Mitochondria
subtype1
subtype2
subtype3
Peroxisome
subtype1
subtype2
subtype3
Lipid Droplets
subtype1
subtype2
subtype3
subtype4
e.
acinus position
PV
CV
H2 distribution
H4 distribution
H5 distribution
H1 distribution
H3 distribution
Frequency
PC2
PC1
f.
scOrganellomics
(N > 3000 cells)
Proportion %
Clusters
Z1
Z2
Z3
Pittsburgh Heterogeneity Indices
Simpson's Index (D)
Shannon's Entropy Index (H)
g.
Proteomics
(N = 390 cells)
Proportion %
Clusters
Z1
Z2
Z3
Pittsburgh Heterogeneity Indices
Simpson's Index (D)
Shannon's Entropy Index (H)

Figure 3.

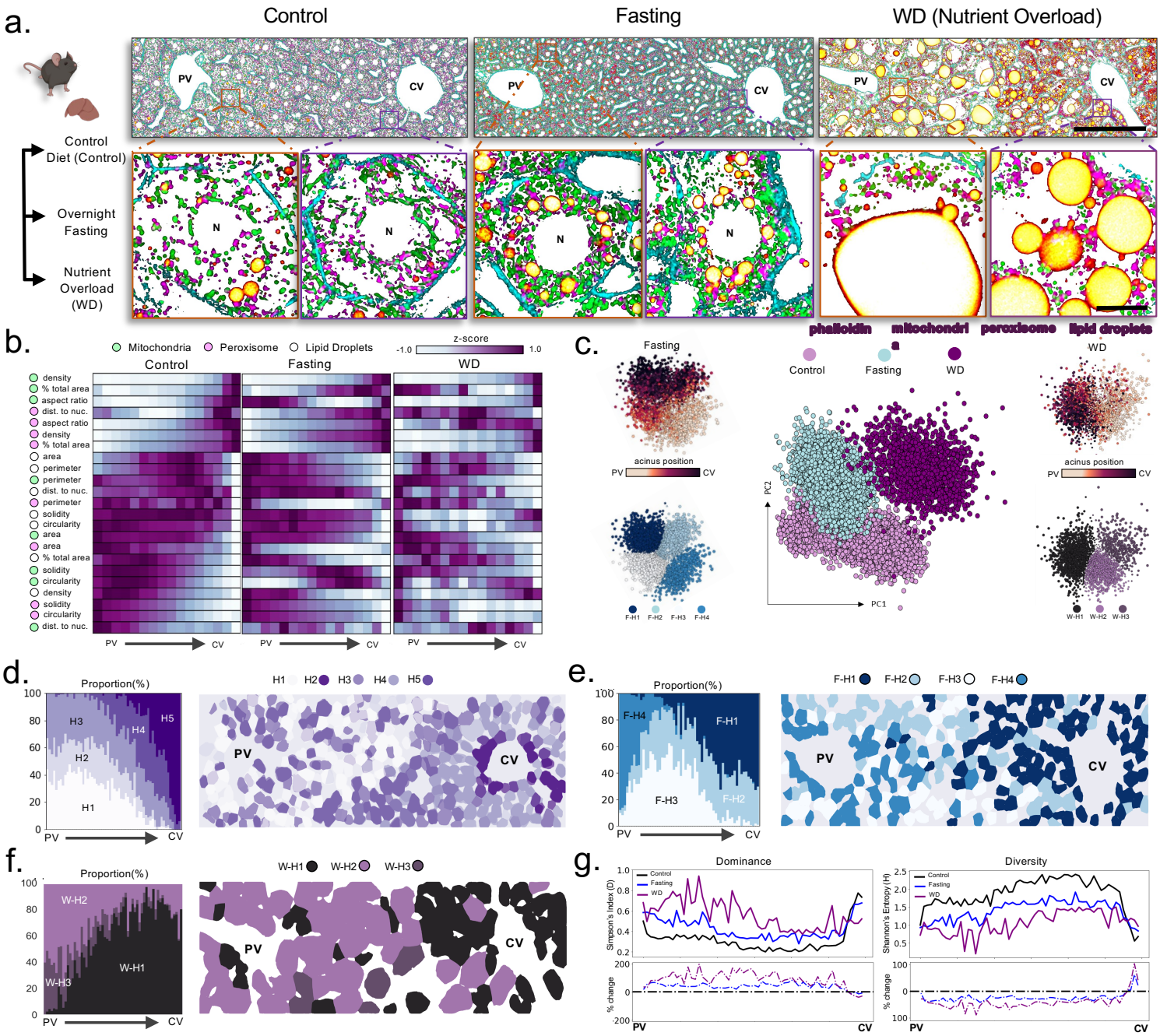
a.
Control
Fasting
WD (Nutrient Overload)
PV
CV
N
Control Diet (Control)
Overnight Fasting
Nutrient Overload (WD)
phalloidin
mitochondri
peroxisome
lipid droplets
b.
Mitochondria
Peroxisome
Lipid Droplets
z-score
-1.0
1.0
Control
Fasting
WD
density
% total area
aspect ratio
dist. to nuc.
aspect ratio
density
% total area
area
perimeter
perimeter
dist. to nuc.
perimeter
solidity
circularity
area
area
% total area
solidity
circularity
density
solidity
circularity
dist. to nuc.
PV
CV
c.
Fasting
acinus position
F-H1
F-H2
F-H3
F-H4
Control
Fasting
WD
PC2
PC1
W-H1
W-H2
W-H3
d.
Proportion(%)
H1
H2
H3
H4
H5
e.
F-H1
F-H2
F-H3
F-H4
f.
W-H1
W-H2
W-H3
g.
Dominance
Diversity
Control
Fasting
WD
Simpson's Index (D)
Shannon's Entropy (H)
% change

Figure 4.

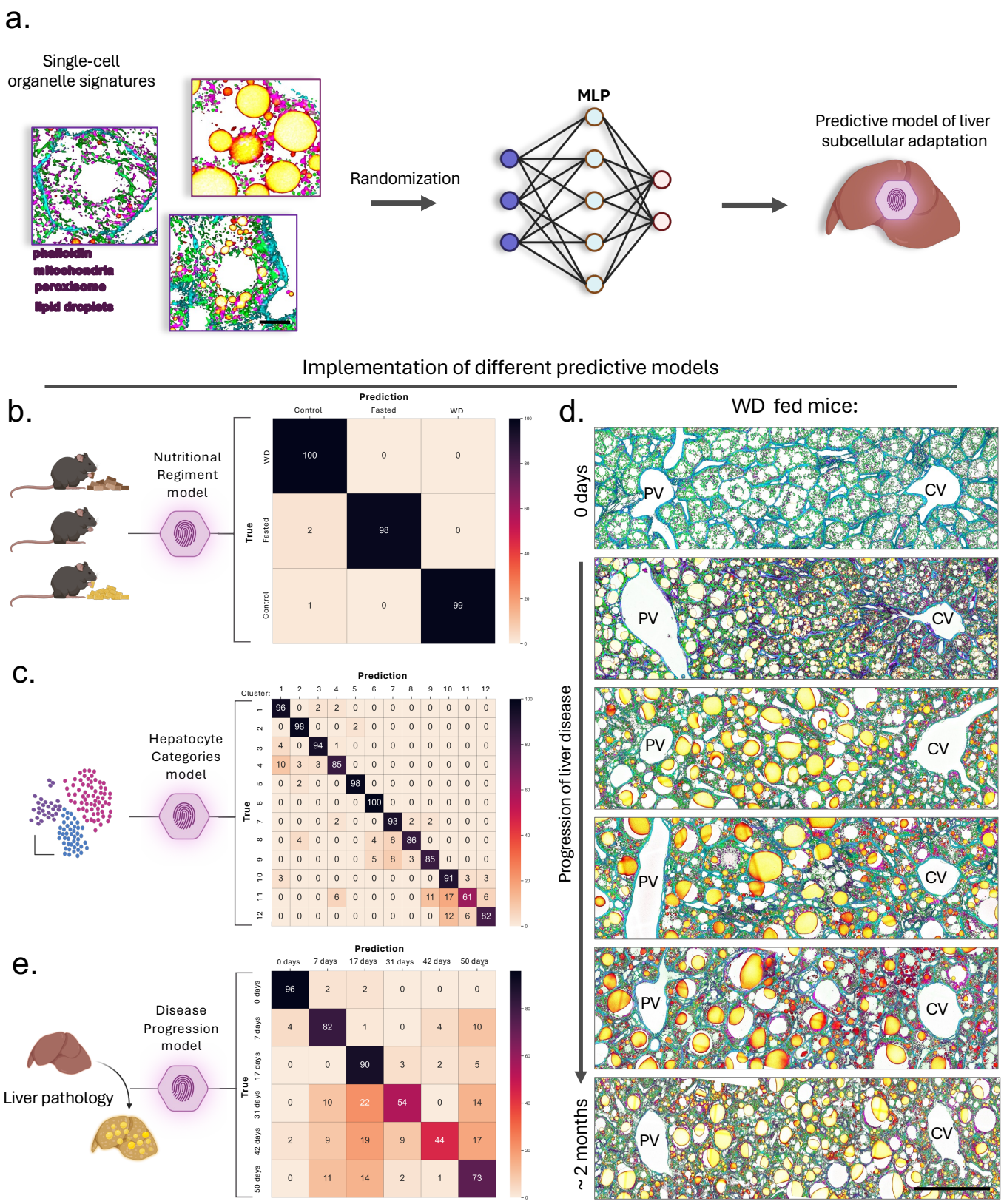
a.
Single-cell organelle signatures
phalloidin
mitochondria
peroxisome
lipid droplets
Randomization
MLP
Predictive model of liver subcellular adaptation
Implementation of different predictive models
b.
Nutritional Regiment model
Prediction
Control
Fasted
WD
True
c.
Hepatocyte Categories model
Cluster:
e.
Disease Progression model
Liver pathology
0 days
7 days
17 days
31 days
42 days
50 days
d.
WD fed mice:
0 days
~ 2 months
Progression of liver disease
PV
CV